CRYSTAL CHEMISTRY OF THREE-COMPONENT WHITE DWARFS AND NEUTRON STAR CRUSTS: PHASE STABILITY, PHASE STRATIFICATION, AND PHYSICAL PROPERTIES

T. A. ENGSTROM, N. C. YODER, AND V. H. CRESPI

Department of Physics, The Pennsylvania State University, University Park, PA 16802, USA; tae146@psu.edu, ncy5007@psu.edu, vhc2@psu.edu

ABSTRACT

A systematic search for multicomponent crystal structures is carried out for five different ternary systems of nuclei in a polarizable background of electrons, representative of accreted neutron star crusts and some white dwarfs. Candidate structures are "bred" by a genetic algorithm and optimized at constant pressure under the assumption of linear response (Thomas–Fermi) charge screening. Subsequent phase equilibria calculations reveal eight distinct crystal structures in the $T = 0$ bulk phase diagrams, five of which are complicated multinary structures not previously predicted in the context of compact object astrophysics. Frequent instances of geometrically similar but compositionally distinct phases give insight into structural preferences of systems with pairwise Yukawa interactions, including and extending to the regime of low-density colloidal suspensions made in a laboratory. As an application of these main results, we self-consistently couple the phase stability problem to the equations for a self-gravitating, hydrostatically stable white dwarf, with fixed overall composition. To our knowledge, this is the first attempt to incorporate complex multinary phases into the equilibrium phase-layering diagram and mass–radius-composition dependence, both of which are reported for He–C–O and C–O–Ne white dwarfs. Finite thickness interfacial phases ("interphases") show up at the boundaries between single-component body-centered cubic (bcc) crystalline regions, some of which have lower lattice symmetry than cubic. A second application—quasi-static settling of heavy nuclei in white dwarfs—builds on our equilibrium phase-layering method. Tests of this nonequilibrium method reveal extra phases that play the role of transient host phases for the settling species.

Key words: dense matter – methods: numerical – plasmas – stars: neutron – white dwarfs

Supporting material: FITS file

1. INTRODUCTION

When an impure white dwarf (WD) or neutron star crust (NSC) is slowly cooled from above its melting temperature, one expects that the extra compositional degrees of freedom are taken advantage of to form crystals that are more efficiently packed than phase-separated body-centered cubic (bcc) lattices. Indeed, several investigators have considered non-Bravais and multicomponent lattices as the possible ground state of astrophysical compact objects. One of the earliest was Dyson (1971), who suggested that a rock salt structure of Fe and He nuclei might be stable. More recently, Kozhberov & Baiko (2012) studied cesium-chloride and magnesium-diboride structures within the Coulomb crystal model. Kobyakov & Pethick (2014) have argued that the ground-state structure above neutron drip density may be similar to that of the displacive ferroelectric $BaTiO_3$, owing to the symmetry-lowering effect of interstitial neutrons on a bcc lattice of nuclei. A related line of inquiry concerns the freezing of multicomponent ion plasmas from the liquid state. See Medin & Cumming (2010) for a semianalytic calculation and references to earlier numerical methods. One such method—classical molecular dynamics—has been used extensively to simulate a multicomponent plasma with the Gupta et al. (2007) composition (Horowitz et al. 2007, 2009; Horowitz & Berry 2009). The latter of these works features a 14-component, $\approx$28,000-particle system that was annealed for $\sim 10^7$ phonon cycles below the melting temperature. A dominantly Se ($Z = 34$) bcc lattice was formed, with small-Z nuclei occupying interstitial positions and larger-Z nuclei acting as substitutional impurities. In addition, there was a tendency for small-Z nuclei to cluster together, forming an

effective large-Z particle. In a different simulation where annealing was again carried out for $\sim 10^7$ phonon cycles (Horowitz et al. 2009), phase-separated regions (microcrystals) formed in the solid phase. One phase was depleted in small-Z nuclei, while another was enriched.

Simulated annealing is an excellent means for directly modeling the dynamics of crystalline systems, but it often cannot access the very long timescales associated with the nucleation and growth of complex multicomponent crystal phases, owing to the exponentially slow dynamics of surmounting reaction barriers against the complex cooperative rearrangements needed to form such crystals. For example, terrestrial carbon steels, which typically have only two to three alloying elements, must be annealed for a minimum of $\sim 10^{13}$ phonon cycles (~ 10 s) to find their ground state (American Society for Metals 1977). Alternative methods, including random structure searching (Pickard & Needs 2011), particle swarm optimization (Wang et al. 2010), and genetic/evolutionary search techniques (Oganov & Glass 2006; Abraham & Probert 2008; Wu et al. 2014), have been applied with great success to this "crystal structure problem," but have not yet been applied at the extreme conditions of compact astrophysical objects. When coupled with an appropriate description of the (fully pressure-ionized) microphysics, such methods could provide a means to efficiently search for new crystal structures in multicomponent WDs and NSCs, complementing the existing simulated annealing work.

The existence of lower-symmetry (i.e., noncubic) and/or multinary phases within WDs and NSCs could have several astrophysical implications. Most astrophysical calculations assume that the material is a bcc polycrystal with grain sizes

small compared to the other macroscopic physical scales in the problem. Therefore, for example, the rank-four elastic tensor is averaged and smoothed to produce a scalar shear modulus relating the strain response to an applied stress (one popular averaging procedure is described by Ogata & Ichimaru 1990). The possibility of multiple, complicated lattice structures and preferential alignment with, e.g., the local magnetic field would necessitate computing the full elastic tensor. Anisotropies, soft phonon modes, and elastic instabilities such as the incipient ones described in Engstrom et al. (2015) could have significant effects on elasticity-related astrophysical observables such as magnetar flares (Perna & Pons 2011), related quasi-periodic oscillations (Israel et al. 2005), and possibly some pulsar glitches (Chamel & Haensel 2008). It could also significantly affect the future observability of gravitational-wave emission, in the context of both magnetar flares and continuous waves (Johnson-McDaniel & Owen 2013). Grain/phase domain boundaries would lead to preferred stress-failure locations and on large scales might affect dissipation of modes involving the crust such as torsion or shear modes (Israel et al. 2005, used to explain quasi-periodic oscillations after magnetar flares) and r-modes (similar to the "crust freezing" scenario in Lindblom et al. 2000). These again would have implications for both electromagnetic and gravitational wave observations. Another kind of implication has to do with the composition of WD debris disks and planetary systems, inferred from metal abundances in the accreting WD's atmosphere (Rafikov 2011; Barber et al. 2012). Entering into this calculation is the settling rate of the high-Z metals. In principle, this rate depends on the buoyancy of the settling species' host phase(s), as well as the microphysics involved in ordinary grain growth processes, namely, interfacial energies and grain boundary mobilities (Krill & Chen 2002). Finally, tightly packed multicomponent crystal structures may lower Coulomb penetration barriers for certain pycnonuclear fusion reactions, characteristically driven by zero-point vibrations of high-density crystals. According to Yakovlev et al. (2006), who consider pycnonuclear reactions in multicomponent plasmas, the reaction rate between a fixed pair of neighboring nuclei is regulated primarily by the exponential factor $\exp(-C\mu d^2\omega)$. Here C is a constant, μ is the reduced mass of the reacting nuclei, d is their equilibrium separation distance, and ω is an effective oscillator frequency coming from phonons. Clearly this reaction rate is extremely sensitive to static and dynamic properties of the specific crystal structure. For example, a high reaction rate may be associated with the small-Z clustering behavior found by Horowitz & Berry (2009) and mentioned earlier in the introduction. In contrast to single-component WD and NSC models, pycnonuclear reaction rates in multicomponent systems are subject to much theoretical uncertainty owing to the ground-state crystal structures (as well as the types of defects supported and the manner in which impurities are absorbed) being largely unexplored (Yakovlev et al. 2006).

In this work we carry out a systematic search for the ground-state crystal structure of three-component (ternary) systems at conditions relevant to WDs and NSCs. The main goals are (1) to identify possible new phases through global search of the multicomponent crystal structure phase diagram and (2) to determine in what contexts those phases might appear in WDs and NSCs through sample applications to layering stability. To the first end, we employ a popular genetic search algorithm. The lowest-enthalpy structures found by the genetic search are included in bulk phase diagram calculations, which reveal five new complicated binary and ternary crystal structures, four having sub-cubic lattice symmetry. To the second end, we demonstrate a self-consistent coupling of the phase stability calculation with the basic equations of a self-gravitating, hydrostatically stable WD. Several compositional instances of the newly found binary phases show up as finite thickness "interphases" between pure bcc strata in cold, He–C–O and C–O–Ne WDs. Additional binary phases make a transient appearance in nonequilibrium settling calculations, as host phases for the settling species.

2. MICROPHYSICS AND STRUCTURAL OPTIMIZATION DETAILS

Our starting point is an effective Hamiltonian for completely pressure-ionized matter. We work within linear response theory —see Section 5 of Pollock & Hansen (1973) and Baiko (2002), for example. In this framework, a system of point nuclei (with charges Z_ie and static positions $\boldsymbol{r}_i$) immersed in a polarizable, charge-compensating background of electrons has kinetic plus electrostatic potential energy

$$E = T_0 + \frac{e^2}{2}\left\{\sum_{i\neq j}Z_iZ_j\int\frac{d^3\mathbf{k}}{(2\pi)^3}\frac{4\pi e^{i\mathbf{k}\cdot(\boldsymbol{r}_i-\boldsymbol{r}_j)}}{\mathbf{k}^2\epsilon(\boldsymbol{k})}\right.$$
$$+\sum_i Z_i^2\int\frac{d^3\mathbf{k}}{(2\pi)^3}\frac{4\pi}{\mathbf{k}^2}\left[\frac{1}{\epsilon(\boldsymbol{k})}-1\right]$$
$$\left.-\sum_{i,j}Z_iZ_j\frac{1}{V}\int d^3\mathbf{r}\int\frac{d^3\mathbf{k}}{(2\pi)^3}\frac{4\pi e^{i\mathbf{k}\cdot\boldsymbol{r}}}{\mathbf{k}^2\epsilon(\boldsymbol{k})}\right\}, \qquad (1)$$

where $\epsilon(\boldsymbol{k})$ is the dielectric function of the electron background (compare Baiko 2002, Equations (1)–(3)). It is not immediately obvious that the above Hamiltonian includes the leading-order correction to the kinetic energy T_0 of the uniform electron gas (it does). This can be seen by expanding the kinetic energy in powers of the density nonuniformity correction, $T = T_0 + \frac{e^2}{2}\int d^3r\, d^3r'\,\delta n_e(\boldsymbol{r})G(\boldsymbol{r}-\boldsymbol{r}')\delta n_e(\boldsymbol{r}')+...$, and keeping only the first two terms such that a total energy minimization identifies $-G(\boldsymbol{k})^{-1}$ as the static response function of the uniform gas. The static response function is in turn related to the dielectric function through $G(\boldsymbol{k})=4\pi k^{-2}(\epsilon(\boldsymbol{k})-1)^{-1}$. Equation (1) also contains all Coulomb interactions except for the infinite nuclear self energies. With a choice of the simple Thomas–Fermi dielectric function $\epsilon_{TF}(\boldsymbol{k})=1+k_0^2/k^2$, the integrals are standard ones and the Hamiltonian reduces to

$$E_{TF} = T_0 + \frac{e^2}{2}\left\{-k_0\sum_i Z_i^2 - \frac{4\pi}{k_0^2 V}\sum_{i,j}Z_iZ_j\right.$$
$$\left.+\sum_{i\neq j}\frac{Z_iZ_j e^{-k_0|\boldsymbol{r}_i-\boldsymbol{r}_j|}}{|\boldsymbol{r}_i-\boldsymbol{r}_j|}\right\}. \qquad (2)$$

In performing structural optimizations, one converges the energy by working with a unit cell of volume V_c and $N-1$ periodic copies thereof. If $\boldsymbol{R}$ is a unit cell translation vector and p, q index the basis (i.e., the specific arrangement of nuclei within the unit cell), the total energy per cell is written as

$$\frac{E_{TF}}{N} = \tau_0 V_c + \frac{e^2}{2}\left\{-k_0\sum_p Z_p^2 - \frac{4\pi}{k_0^2 V_c}\sum_{p,q} Z_p Z_q \right. \\ \left. + \sum_{R,p,q}{}' \frac{Z_p Z_q e^{-k_0 \mathscr{R}_{pq}}}{\mathscr{R}_{pq}}\right\}, \qquad (3)$$

where $\mathscr{R}_{pq} = |\boldsymbol{R} + \boldsymbol{r}_p - \boldsymbol{r}_q|$ and the prime on the last sum indicates that terms with $\mathscr{R}_{pq} = 0$ are excluded. For this work we use kinetic energy density

$$\tau_0 = \frac{1}{8\pi^2}\frac{m_e c^2}{\lambda_e^3}\left[\frac{x^2(1+2x^2)}{\beta} - \ln\left(x+\frac{x}{\beta}\right)\right] - m_e c^2 n_e, \qquad (4)$$

and screening length

$$k_0^{-1} = \frac{\lambda_e}{2x}\sqrt{\frac{\pi\beta}{\alpha}}, \qquad (5)$$

corresponding to the relativistic, degenerate gas. Here $\lambda_e = \hbar/m_e c$ is the reduced Compton wavelength, $x = p_F/m_e c = \lambda_e(3\pi^2 n_e)^{1/3}$, $\beta = x/\sqrt{1+x^2}$, and $\alpha \approx 1/137$ is the fine-structure constant. The Thomas–Fermi description breaks down when the screening length localizes electrons to within their Compton wavelength; this occurs for $x \gtrsim 10$ ($\rho \gtrsim 10^9$ g/cc). Approaching this extreme relativistic limit, the ratio of screening length to the characteristic distance between nuclei $r_s = (3\langle Z\rangle/4\pi n_e)^{1/3}$ tends to a constant (for a bcc lattice of Fe nuclei, the constant is 1.82), so we might anticipate that phase boundaries become stationary in this scale-invariant limit. Saturation of k_0^{-1}/r_s at this small value is indicative of the overscreening predicted by the Thomas–Fermi model. Within these constraints, however, the model has the advantage of being both reasonably accurate and computationally efficient, readily incorporated into a global search of crystal structure and composition.

Structural optimizations using Equations (3)–(5) are conveniently carried out at constant volume—one need only minimize a pairwise sum of effective Yukawa interactions, which converges rapidly in real space for $k_0^{-1}/r_s \sim 1$. Because it will prove useful for the phase-layering calculation described later, we choose instead to perform structural optimizations at constant external pressure P and minimize the enthalpy. This can be accomplished using a modified version of the General Utility Lattice Program (GULP; Gale & Rohl 2003), where the Yukawa interaction (available as a special case of the "general" pair potential) is given the capability to handle a V_c-dependent screening length. We modify GULP's enthalpy per unit cell to $h_{TF} = E_{TF}/N + PV_c$, and the first strain derivatives of the enthalpy (sufficient for steepest descents and conjugate

gradient methods) are accordingly modified to

$$\frac{\partial h_{TF}}{\partial\epsilon_{\alpha\beta}} = \left[(P - P_0)V_c + \frac{2\pi e^2(2-\beta^2)}{3k_0^2 V_c}\sum_{p,q}Z_p Z_q \right. \\ \left. + \frac{e^2 k_0(1+\beta^2)}{12}\sum_{R,p,q}Z_p Z_q e^{-k_0\mathscr{R}_{pq}}\right]\delta_{\alpha\beta} \\ - \frac{e^2}{2}\sum_{R,p,q}{}'\frac{Z_p Z_q\,\mathscr{R}_{pq}^\alpha\,\mathscr{R}_{pq}^\beta\,e^{-k_0\mathscr{R}_{pq}}}{\mathscr{R}_{pq}^2}\left(k_0 + \frac{1}{\mathscr{R}_{pq}}\right), \quad (6)$$

where $P_0 = n_e^2\partial(\tau_0/n_e)/\partial n_e$ is the kinetic pressure of the uniform electron gas. Derivatives of h_{TF} with respect to GULP's remaining degrees of freedom (fractional basis coordinates) are not affected by $k_0 \to k_0(V_c)$.

3. GENETIC SEARCH PROGRAM FOR DETERMINATION OF THE $T = 0$ BULK PHASE DIAGRAMS

This section describes a global search of composition and structure, using five ternary systems of nuclei thought to be relatively prevalent in WD or NSC matter, and covering a range of distinct crystal chemistries: He–C–O, C–O–Ne, C–O–Fe, O–Fe–Se, and Fe–As–Se. The first two ternary systems are relevant to WDs, likely including those that are Type Ia supernova (SN Ia) progenitors (Shen & Bildsten 2014). The third may also be relevant to WDs having undergone a failed-detonation SN Ia (Jordan et al. 2012). The rationale for choosing the remaining two is that these particular nuclei are representative and/or prevalent among the Gupta et al. (2007) abundances near neutron drip. Incorporating a full list of abundances ($\approx$17 species) would be intractable for the type of calculation described in this work. Moreover, we can take a lesson from Earth-condition crystals, which typically have only one, two, or three elements (sometimes four). This appears to be due to general properties of crystal stability related to phase separation of complex unit cells: basically, once a structure reaches a sufficient level of complexity that it can accommodate the special geometrical characteristics of its constituent atoms, it is disadvantageous to make the unit cell any larger (in the sense of adding more atoms), since that just reduces the amount of favorable repetition possible with a given number of atoms. Exploring more ternary combinations is also likely to give diminishing returns in the prediction of new structures. Roughly speaking, with a smooth and spherically symmetric interaction such as the Yukawa potential, there are only four qualitatively different ternary combinations: one big Z and two small Zs, two big and one small, all three mismatched, and all three similar. As long as the screening length regimes (characterized by k_0^{-1}/r_s) are not too different, one expects to see a continuity of structures formed by systems having similar relative Zs (or perhaps squared Zs), since in the case of complete pressure ionization there are no complex crystal chemistry effects due to covalent bonding, rehybridization, or the filling of atomic orbitals. Another reason for studying the specific ternary systems mentioned above is that they cover at least three (arguably all four) of the qualitatively different combinations.

We carry out ground-state structure searches at a series of pressures and stoichiometries (relative amounts of different nuclei), enumerated below, using the evolutionary crystal

structure prediction software XtalOpt r8.0 (Lonie & Zurek [2011]) together with GULP optimization.[1] XtalOpt first generates a pool of random structures all having the desired stoichiometry. Each of these zeroth-generation structures is optimized to its local free energy minimum (as described in the previous section) and evaluated for "fitness"—essentially a probability of breeding based on enthalpy relative to sibling structures. Fit parents are operated on in one of three distinct ways in an attempt to generate even fitter (lower enthalpy) offspring. One type of operation involves cutting and splicing two parent unit cells by expressing the locations of each atom within the unit cell (i.e., the basis vectors) in terms of lattice coordinates (i.e., linear combinations of the three lattice vectors with weights all less than one) and then taking one fraction of the unit cell from one parent and the remaining fraction from the other. The remaining two genetic operations involve a single parent: one combines particle permutations with a homogeneous strain; the other combines a homogeneous strain with a cosine deformation. Parameters in each of these operational elements are chosen from uniform random distributions. The optimizer is again called on to relax the child structures, and the process is iterated for many generations.

For simplicity, we assume that the WD/NSC ground state is a polycrystalline mixture of stoichiometric compounds. A stoichiometric compound is here defined to be a periodic solid in which stoichiometry does not vary across unit cells. Notably excluded from our analysis are alloy phases (e.g., those with disordered occupation of the lattice sites by more than one atom type), and we further restrict to a subset of the possible stoichiometric compounds. For a given ternary system of nuclei A–B–C, a constant pressure search is performed at $P = 10^{11}$ and 10^{16} GPa for each of the nominally 125 stoichiometries $A_n B_m C_\ell$ where $n, m, \ell = 0 \ldots 4$. Search cells with small number of particles $n + m + \ell$ are removed from the search program if they are submultiples of larger cells; thus, there are 98 searches per ternary system, per pressure. Each of these searches is run out to at least 480 optimized, genetically operated-on structures, except in the case of single-component searches, which are run out to at least 80 optimized structures (the first 20 seed structures are randomly generated). Lattice sums are done in real space with cutoff $\approx 20 k_0^{-1}$ and are expected to be converged to seven to eight digits. This level of accuracy is important, as we find that enthalpies of competing structures can be the same out to six digits. Default XtalOpt search parameters are used throughout, and following the suggestions put forth in the XtalOpt implementation paper (Lonie & Zurek [2011]), we benchmark the search parameters by constructing Hartke plots for several relativistic screened-Coulomb systems (see Figure [1]). Hartke plots gauge the performance of a genetic search and help establish a stopping criterion. Our choice of search duration, previously mentioned, is in part motivated by the "Hartke lifetimes" found in these tests.

The lowest-enthalpy structure found in each search is included in a bulk phase stability calculation, such as that performed by Thermo-Calc software (Andersson et al. [2002]).
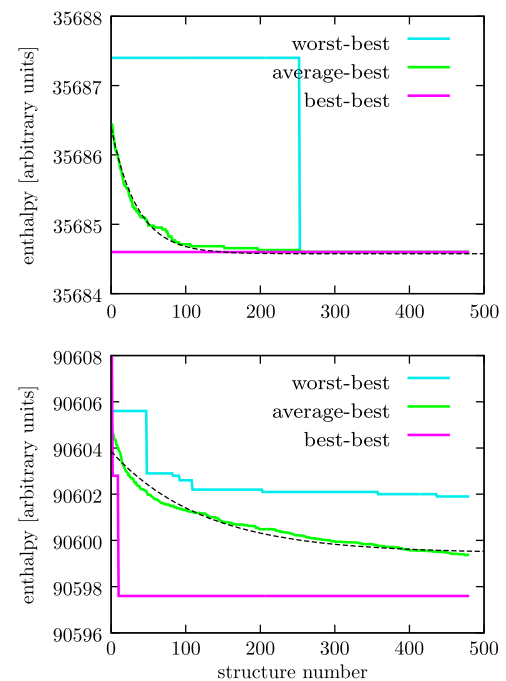

Figure 1. Hartke plots for search cells FeO_3C_2 (top) and $Fe_4O_4C_4$ (bottom). $y(x)$ is the enthalpy of the lowest-enthalpy structure found within the range of structure numbers: zero to x. The initial 20 seed structures (randomly generated by XtalOpt) are not included; thus, the Hartke plot contains information only about structures that have been genetically operated on. For each plot, 100 runs were made with identical parameters. In the case where all runs eventually found the same lowest-enthalpy structure (top), the worst–best is the single run that took the longest to find it. In the case where not all runs found the same lowest-enthalpy structure (bottom), the worst–best is the single run whose winning structure had the highest enthalpy. Best–best was the quickest to find the overall lowest-enthalpy structure, and average–best is the average over all 100 runs. The Hartke lifetimes associated with the exponential fits to average–best (black dashed lines) are 35 (top) and 123 (bottom). The winning structure found in the FeO_3C_2 search appears in the bulk phase diagram, as the η phase. The $Fe_4O_4C_4$ search has the most degrees of freedom out of any search cell in our program; its winning structure does not appear in the phase diagram.

For a given set of $N_C + 2$ state variables (N_C being the number of components) Thermo-Calc finds the global minimum Gibbs free energy that lies on a plane tangent to the available phases' Gibbs energy surfaces. A phase diagram representable as a 2D plot is then constructed from the set of tangent planes found by varying any two of the state variables. (For a pedagogical reference to phase diagrams, see the book by Hillert [2007].) Since all the phases considered in this work are stoichiometric compounds, there is a simplification in that the phases' Gibbs energy surfaces are themselves points. Consequently, in this work, any point within a ternary phase diagram is a point at which three different phases coexist as a polycrystalline mixture (unless the point happens to be on a phase boundary, in which case two phases coexist). If a structure appears in the equilibrium phase diagram at either $P = 10^{11}$ or 10^{16} GPa, it is reoptimized at intermediate-pressure decades to obtain the pressure dependence of the phase diagram. It is possible, though unlikely, that there are phases stable only over a narrow band of pressure that are missed by this procedure (the full search scheme was carried out for the C–O–Fe system at several intermediate pressures and found no such "missed" phases, lending support to this approach). Finally, we mention the single exception to the search program described above: in the He–C–O system, real-space lattice sums converge much

---

[1] It is convenient to reinterpret XtalOpt and GULP's internally consistent (eV, Å, GPa) unit system as $(10^d \text{ eV}, 10^{-d} \text{ Å}, 10^{4d} \text{ GPa})$, so that issues with numerical limits can be avoided. These codes were, of course, originally intended for Earth-condition materials! Useful choices of the integer d include 2, 3, and 4. In this scheme, the relativity parameter appearing in Equations ([4]) and ([5]) becomes $x = 1.1946484 \times 10^{4d-2} n_e^{1/3}$, and the prefactor in Equation ([4]) becomes $m_e c^2 / 8\pi^2 \lambda_e^3 = 1.1239083 \times 10^{11-4d}$.
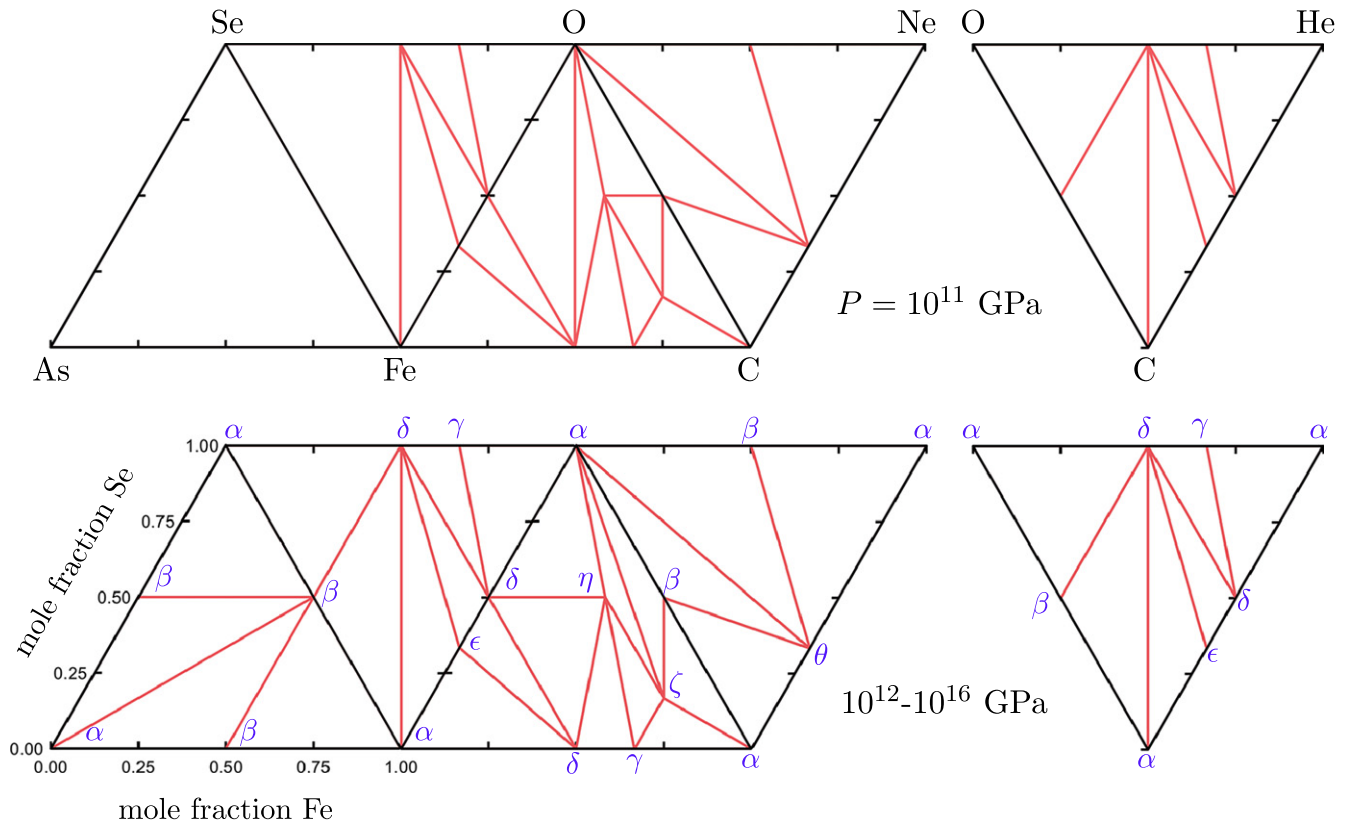
Figure 2. $T = 0$ bulk phase diagrams for relativistic screened-Coulomb systems. Each pair of vertically aligned diagrams corresponds to a specific ternary system of nuclei, while the two rows give the pressure dependence. Across the five ternary systems investigated, no pressure dependence was found in the range 10^{12}–10^{16} GPa, despite the fact that the screening length k_0^{-1} varies considerably over this range (from $1.36 r_s$ to $1.81 r_s$ for bcc Fe). Following from our assumptions described in the main text, the microstructure within a given triangular region is a polycrystalline mixture of the three stoichiometric compounds (phases) indicated at the triangle's vertices. At points on a red line (phase boundary), the microstructure is a polycrystalline mixture of the two phases indicated at the line's endpoints (an intersection with a black line defines an endpoint, in the space-saving representation above). All distinct phases are labeled with Greek letters and explained in Table 1.

more slowly than in the other systems owing to the larger k_0^{-1}/r_s, so the full 98 searches are carried out only at $P = 10^{11}$ GPa.

4. BULK PHASE DIAGRAM RESULTS

While pressure invariance of the $T = 0$ phase diagram was anticipated in the extreme relativistic limit, it comes as some surprise that the pressure independence persists well below this limit, nearly to the threshold for full pressure ionization. Figure 2 shows that for all five ternary systems studied, no P-induced phase transitions were found above 10^{12} GPa. For bcc Fe, this pressure corresponds to density 6.18×10^5 g/cc and screening length $k_0^{-1}/r_s = 1.36$, or about 75% of the saturation value. In general, screening length on the order of the lattice spacing appears to be a requisite for P-driven phase transitions. Further supporting this conclusion is the fact that the He–C–O and C–O–Ne systems do not undergo any pressure-induced transitions in the range 10^{11}–10^{16} GPa; within that range, screening lengths in these small-Z systems are significantly larger than one lattice spacing.
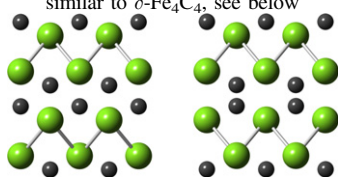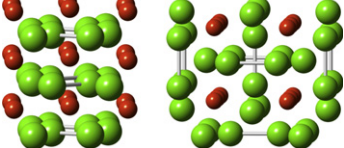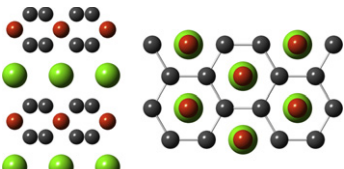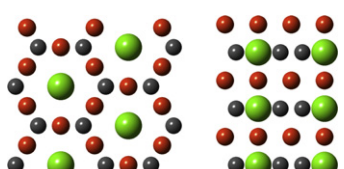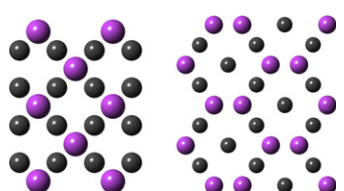
Another finding is that combinations of nuclei with significantly mismatched Zs are much more conducive to efficient multicomponent packings than are systems where the Zs are fairly similar. For example, the Fe–As–Se system has an extremely simple low-pressure phase diagram: at any composition, the microstructure consists simply of phase-separated bcc crystallites. Multicomponent phases appear at high pressure,

but they have the simple cesium-chloride structure. In contrast, the C–O–Fe phase diagram is quite rich. Combining one large Z and two smaller Zs results in a variety of binary and ternary crystal structures (enumerated in Table 1), all of which are more efficient (have a higher packing fraction) than phase-separated bcc lattices.

Both He–C–O and O–Fe–Se systems (two large, one small) feature all the same phases as C–O–Fe, except for the two ternary compounds that do not appear. While a continuity of structures appearing between these systems was anticipated, it is striking that at high pressures the two phase diagrams are identical. Close similarity is also noted between the Fe–As–Se and C–O–Ne systems, which both consist of three similar Zs. The outlier in this comparison is the nontrivial C–Ne binary structure, described in Table 1. These observations are consistent with the idea that it is the combination of relative Zs, and not of absolute Zs, that is important in determining the high-pressure phase diagram.

In the pressure and screening length regimes appropriate to this work (while P ranges from 10^{11} to 10^{16} GPa, k_0^{-1}/r_s ranges from 1.13 to 1.81 for bcc Fe), there is a competition between close packing and next-nearest-neighbor interactions, which the closest packed structures tend not to win. This is exemplified by bcc's favorability over face-centered cubic (fcc), and the fact that only one of the equilibrium phases found (magnesium-diboride structure) also appears in the phase diagram of densest binary sphere packings (Hopkins et al. 2011, 2012). The simplest multicomponent crystals have structures that are also

Table 1
Selected Compounds Appearing in the C–O–Fe and C–O–Ne Bulk Phase Diagrams, as Indicated in Figure 2

Phase Label	Unit Formula	Crystallographic Space Group or Structure	Relative Proton Density	Relative Baryon Density[a]	Density Relative to Bulk, Phase-separated bcc[b]	Views along (or Slightly Oblique to) Some High-symmetry Directions
α	Fe	bcc	1	1	1	
α	O	bcc	0.982	0.912	1	
α	C	bcc	0.980	0.910	1	
β	OC	cesium-chloride	0.981	0.911	1.000001	
γ	FeC_2	magnesium-diboride	0.994	0.971	1.000061	
δ	Fe_4O_4	Cmcm (orthorhombic)	0.996	0.979	1.000040	similar to δ-Fe_4C_4, see below
δ	Fe_4C_4	Cmcm (orthorhombic)	0.996	0.983	1.000056	
ϵ	Fe_4O_2	I4/mcm (tetragonal)	0.998	0.988	1.000024	
ζ	$FeOC_4$	P6/mmm (hexagonal)	0.989	0.950	1.000044	
η	FeO_3C_2	P6/mmm (hexagonal)	0.989	0.948	1.000039	
θ	Ne_2C_4	Fd−3 m (cubic)	0.997	0.997	1.000021	

Notes. All numerical values given here correspond to $P = 10^{16}$ GPa. Relative proton density is a measure of geometrical packing efficiency; relative baryon density includes the nongeometrical effect of neutron fractions. The reference phase for these relative densities is α-Fe, except in the case of θ-Ne_2C_4, for which the reference phase is α-Ne. Renderings have gray C, red O, green Fe, and violet Ne, with sphere volume proportional to the nuclear charge Z. In the δ and ϵ renderings, bonds indicate Fe–Fe the first nearest neighbors. If the space group is listed instead of a specific crystal structure, the unit formula gives the composition of the search cell in which the structure was found, not necessarily that of the primitive cell. Pdb files of the structures (for all compositional instances) are included as supplementary materials in the online version.
[a] Using ^{12}C, ^{16}O, ^{20}Ne, and ^{56}Fe.
[b] Defined as the sum of cell volumes after phase separation into bulk bcc phases, divided by the original cell volume.
(This table is available in its entirety in FITS format.)

assumed by some ionic compounds under low-pressure conditions, which may reflect the fact that ionic solids have a simple close-shell electronic structure (ionic solids also have strong $+/-$ Coulomb interactions that are missing here). When a pair of Zs are not too dissimilar, they usually form the cesium-chloride structure, e.g., OC, NeO, SeFe, SeAs, and AsFe. When they are more dissimilar, they tend to form magnesium-diboride structure, e.g., OHe_2, FeC_2, and SeO_2.

Magnesium diboride is our first encounter with sub-cubic symmetry, which could give rise to transport anisotropy, elastic anisotropy, and other effects such as a magnetic field coupling to the structure orientation. A quite prevalent but more complicated orthorhombic structure occurs at chemical compositions O_4He_4, C_4He_4, Fe_4O_4, Fe_4C_4, and Se_4O_4, where these different instances can be interconverted by small adjustments of bond lengths and angles. A tetragonal structure occurs at

compositions C_4He_2 and Fe_4O_2; this is the second-highest density structure in the C–O–Fe system and could potentially drive oxygen to greater depths than it would otherwise go. The C–O–Fe system also features two ternary structures $FeOC_4$ and FeO_3C_2, both with hexagonal symmetry. $FeOC_4$ can be viewed as magnesium-diboride structure, with the triangular magnesium planes alternating between Fe and O compositions. FeO_3C_2 consists of alternating layers of kagome O and honeycomb C, with Fe at the holes in the honeycomb layers.

A general feature of the the ternary bulk phase diagrams is that coexisting phases have mass density differences, owing to a combination of neutron fraction and geometrical packing effects. These differences can be as large as $\sim 10\%$ of the total density and will result in stratification of phase domains in the presence of a gravitational field—the problem to which we now turn.

5. EQUILIBRIUM-LAYERING CALCULATION

Here we give an application of our high-pressure crystal chemistry results to WDs at a given fixed overall composition. The equilibrium phase-layering diagram of a zero-temperature WD is computed self-consistently, allowing for arbitrary numbers of components N_C and phases N_P that can be formed from these components. The problem is decomposed into two parts: one part is a microscopic phase stability calculation that produces a function $\rho(h)$, where ρ is density and h is enthalpy per unit mass; the other is a simple stellar structure calculation that determines the pressure–radius dependence $P(r)$. We iterate between these two parts. The former is inspired by a technique used among chemical engineers to study species segregation in oil reservoirs (see Esposito et al. 2000).

In the following, we will make use of the virial theorem for the gravitational potential energy W of a WD, given by

$$W = -3 \int_0^R P \, 4\pi r^2 dr. \qquad (7)$$

We begin by discretizing the star into N_L onion layers of uniform thickness $\Delta r = R/N_L$. If Δr is small compared to the scale height of pressure $H_P = -dr/d \log P$, the ith layer may be treated as a bulk equilibrium system at constant pressure P_i, and one may work with the modified Helmholtz free energy

$$F^* = \sum_{i=1}^{N_L}\left[-4P_i V_i + \sum_{\alpha=1}^{N_P} n_{\alpha i}\, \mu_\alpha(T, P_i)\right]. \qquad (8)$$

For each term in the sum over layers, $-3P_i V_i$ comes from the discrete version of Equation (7), and another $-P_i V_i$ cancels the corresponding quantity in the Gibbs free energy of the layer, $\sum_\alpha n_{\alpha i}\, \mu_\alpha(T, P_i)$. Here $n_{\alpha i}$ is the (unknown) molar amount of phase α present in layer i, and μ_α is the bulk chemical potential of phase α. (The phase index α is not to be confused with the bcc structure, as in Table 1.) We have thus avoided the complication of introducing a gravitational term into the chemical potentials, including it instead at the level of the layers. This comes at the cost of supplying a pressure function $P(r)$ consistent with hydrostatic equilibrium, implicit in Equations (7) and (8). Let us assume that we have such a pressure function. (For an initial guess, we will take $P(r)$ from an $n = 3$ polytrope.) Now fix a set of layer pressures $P_i = P(i\Delta r)$. The problem of minimizing F^* has been reduced

to the problem of minimizing the linear objective function $\sum_i \sum_\alpha n_{\alpha i}\, \mu_\alpha(T, P_i)$, subject to $2N_L + N_C - 1$ constraints

$$1 = \frac{1}{V_i} \sum_\alpha \frac{n_{\alpha i}\, m_\alpha}{\rho_\alpha(T, P_i)} \quad \text{for } i = 1 \ldots N_L, \qquad (9)$$

$$0 = \sum_{i,\alpha}[(1 - x_A)s_{A\alpha} - x_A s_{B\alpha} - x_A s_{C\alpha}]n_{\alpha i}, \qquad (10)$$

$$\text{etc. for } x_B \ldots x_{N_C},$$

$$0 \geqslant \sum_\alpha \left[\frac{n_{\alpha i+1}}{V_{i+1}} - \frac{n_{\alpha i}}{V_i}\right]m_\alpha \quad \text{for } i = 1 \ldots N_L-1, \qquad (11)$$

each of which is also linear in the $n_{\alpha i}$. The first set of constraints ensures that the volume filling fraction is equal to 1 for each layer, where the molar mass m_α and density $\rho_\alpha(T, P_i)$ are assumed to be known for each phase. Equations (10) constrain the global mole fractions $x_A \ldots x_{N_C}$, where, for example, $s_{A\alpha}$ specifies the number of A-type nuclei per formula unit of the α phase. The reason for constraining mole fractions rather than component masses is that the latter tends to cause infeasibility problems for the Simplex solver. Finally, there is a set of inequality constraints that guarantees the reality of the interlayer Brunt-Väisälä frequencies $\omega = \sqrt{-(g/\rho)(d\rho/dr)}$. Thus, there is built-in stability against convective overturn of adjacent layers, but note that it is still possible to have unstably stratified material *within* a layer. As noted above, this problem is straightforwardly solved using the Simplex method. For number of variables $N_L N_P \sim 10^3$–10^4, we use the high-performace lp_solve routines.

So far we have considered the case of an isothermal WD. For the special case $T = 0$, the Simplex solution provides the layer enthalpy per unit mass $h_i = \sum_\alpha n_{\alpha i}\, \mu_\alpha(0, P_i)\big/\sum_\alpha n_{\alpha i} m_\alpha$ and layer density $\rho_i = \sum_\alpha n_{\alpha i} m_\alpha\big/V_i$. In certain cases, one can interpolate to obtain a smooth function $\rho(h)$, which can be combined with the enthalpy-transformed stellar structure equations (Lindblom 1992).[2] In the nonrelativistic limit, these read

$$\frac{dP}{dh} = \rho, \qquad (12)$$

$$\frac{dm}{dh} = \frac{-4\pi r^4 \rho}{Gm}, \qquad (13)$$

$$\frac{dr}{dh} = \frac{-r^2}{Gm}. \qquad (14)$$

The reason for using the enthalpy transformation is twofold. First, the total mass M, which we were not able to constrain in the Simplex calculation, now enters as a boundary condition. Second, if we simply used the layer masses $M_i = \sum_\alpha n_{\alpha i} m_\alpha$ along with the discretized equations of mass continuity and

---

[2] An issue can arise near a density discontinuity, where h_i and ρ_i obtained by the above procedure describe a function $h(\rho)$ that is nonmonotonic. The stellar structure calculation cannot then make use of the enthalpy transformation, because the sign of Equation (14) is incorrect in the vicinity of the interface. A density discontinuity occurs as a consequence of mismatched Zs (compare bcc C and O in Table 1) but is made much more severe when there is also a mismatch in neutron fraction (compare bcc O and Fe in Table 1). Fortunately, for typical WD compositions, the neutron fraction is continuous (or nearly so) across phase boundaries, and the issue of nonmonotonicity is avoided by choosing a suitably large layer thickness—on the order of $R/200$ for He–C–O and C–O–Ne compositions.

hydrostatic equilibrium (the usual stellar structure equations) to update the P_i, no information about the microscopic energy scale would carry over. In other words, we could multiply all the chemical potentials by 2 and get the same P_i. Equations (12)–(14) are to be integrated inward from the boundary conditions $P(0) = 0$, $m(0) = M$, and $r(0) = R$. Unfortunately, we have no a priori knowledge of the radius R that is consistent with M and $\rho(h)$ in the sense of the Oppenheimer–Volkoff map (to use the language of Lindblom). We therefore have to complete the mapping $\rho(h) \mapsto (M, R)$. A simple way to accomplish this is by "aiming" the boundary condition $r(0)$ until the integration yields the physically correct behavior $dP/dr = 0$ as $r \to 0$. Approaching R from below, the solutions are smooth and well behaved except at $r = 0$ owing to a singularity in Equation (14). A change of variable $u = r^2$ removes this singularity, but we find no particular advantage to working with the resulting transformed equations. Approaching R from above generates sign changes, and the solutions are generally chaotic. The qualitatively different behaviors in these two regimes can be exploited to obtain R to arbitrarily high precision. In practice, we minimize dP/dr at a fixed, small fraction of the starting boundary condition $r(0)$ (but see the next paragraph for discussion of a special case). In this process of "completing the map," an updated pressure function $P(r)$ is obtained at no extra cost. Layer pressures are reassigned and input to the Simplex calculation and the process iterated. One choice of convergence criterion is that successive iterations produce stellar radii that are the same to within a tolerance of $10^{-6} R_\odot$—typically this criterion is met within just a few iterations. Another choice is that radial positions and thicknesses of phase strata (as fractions of R) are static to within the resolution set by the number of simulation layers—typically this occurs after just one iteration.

The main type of numerical error incurred is of the following nature. In the first iteration, integration of Equations (12)–(14) never proceeds past the point for which we have tabulated h_i, ρ_i data available to interpolate within. This is just a consequence of having used the polytrope initial guess. In subsequent iterations, however, we are sometimes forced to make a choice: carry out the integration past the highest tabulated h_i, replacing interpolations with extrapolations, or simply terminate the integration when interpolations become impossible, using the current value of dP/dr in the aiming procedure discussed above. We choose the second option. The minimization problem within the aiming procedure is, in these cases, somewhat ill defined, tending to generate some numerical noise that is expressed in the layering diagram near $r/R = 0$. For this reason we present layering diagrams as they appear after the first iteration, noting that changes to the layering diagram are already nearly imperceptible by the second iteration, save for an increase in the level of this numerical noise.

6. EQUILIBRIUM-LAYERING RESULTS

The previous section described a method of determining the radial positions and amounts of phase strata in a WD with fixed mass and overall composition, in particular, strata composed of the new multicomponent crystal structures. Using this method,

we computed the $T = 0$ equilibrium phase-layering diagrams and radius-composition dependence of 1.0 solar mass, ^{4}He–^{12}C–^{16}O and ^{12}C–^{16}O–^{20}Ne WDs. For each composition, an initial guess corresponding to the polytrope $P = 3.8 \times 10^{14} \rho^{4/3}$ cgs and stellar radius $R = 7.5 \times 10^{-3} R_\odot$ was used, although the method appears to converge to the same result if these starting values are adjusted within reasonable limits. Figure 3 shows the result of the calculation. Evidently, pure bcc phases make up the majority of the stellar interior, despite the multicomponent structures being more efficiently packed. Since multicomponent phases tend to show up at interfaces, we refer to them as "interphases." In the He–C–O star, for example, δ-C$_4$He$_4$ and ϵ-C$_4$He$_2$ interphases are formed between α-C and α-He, while β-OC appears at the low-density part of the C–O boundary. For compositions near $x_{He} = 1$, the thinness of the carbon shell allows O-He interphases to form, namely, γ-OHe$_2$ and δ-O$_4$He$_4$. Compared to sharp bcc–bcc interfaces, interphases offer free energy savings owing to optimized crystal packing density, nearest- and next-nearest-neighbor interactions, etc., arising from the extra compositional degrees of freedom. Interphase thinness relative to bcc strata can be understood from the gravitational contribution to the free energy having a tendency to "pull apart" the different Z components of the multicomponent phases. Competition between these two energy scales apparently causes interphases to become slightly thicker with depth. Consider, for example, δ-C$_4$He$_4$ in the diagram with $x_O/x_C = 1$. At $x_{He} = 0.5$, only one simulation layer (out of 200) is completely filled with this compound, while an adjacent layer contains a mixture of δ-C$_4$He$_4$ and α-He. This interphase gradually thickens with x_{He} and by $x_{He} = 0.95$, 13 simulation layers are completely filled, another two are partially filled, and δ-C$_4$He$_4$ has squeezed out α-C from the layering diagram.

An unexpected but apparently generic feature of the radius-composition curves in Figure 3 is the existence of a shallow minimum of the WD radius at an impure composition. Even as the level of numerical noise increases with further iterations, this minimum clearly persists. The cusps near $x_{He} = 0.8$ and $x_{Ne} = 0.3$ may be a numerical effect rather than a physical one, however, as they tend to smooth out upon further iterations.

One expects that the physics driving interphase formation in our sample calculations for WDs would also drive interphase formation in multicomponent NSCs. Complex accreted crusts, with number of components $\gg 3$, may well have a larger number of interphases than the few that were found here for three-component WDs. The amount of interphase material relative to pure bcc material could also be larger. In addition, if some components are present only in trace amounts, their associated bcc strata may be thin or even nonexistent, enabling mixing of the species above and below and formation of interphase crystals containing more than two components. These arguments would also apply to multicomponent WDs, perhaps including some of those discussed in Barber et al. (2012) and Jordan et al. (2012).

7. EXTENDING THE EQUILIBRIUM CALCULATION: A TOY MODEL OF NONEQUILIBRIUM PHASE LAYERING

A simple modification of the equilibrium-layering calculation enables a quasi-static settling calculation. If the settling
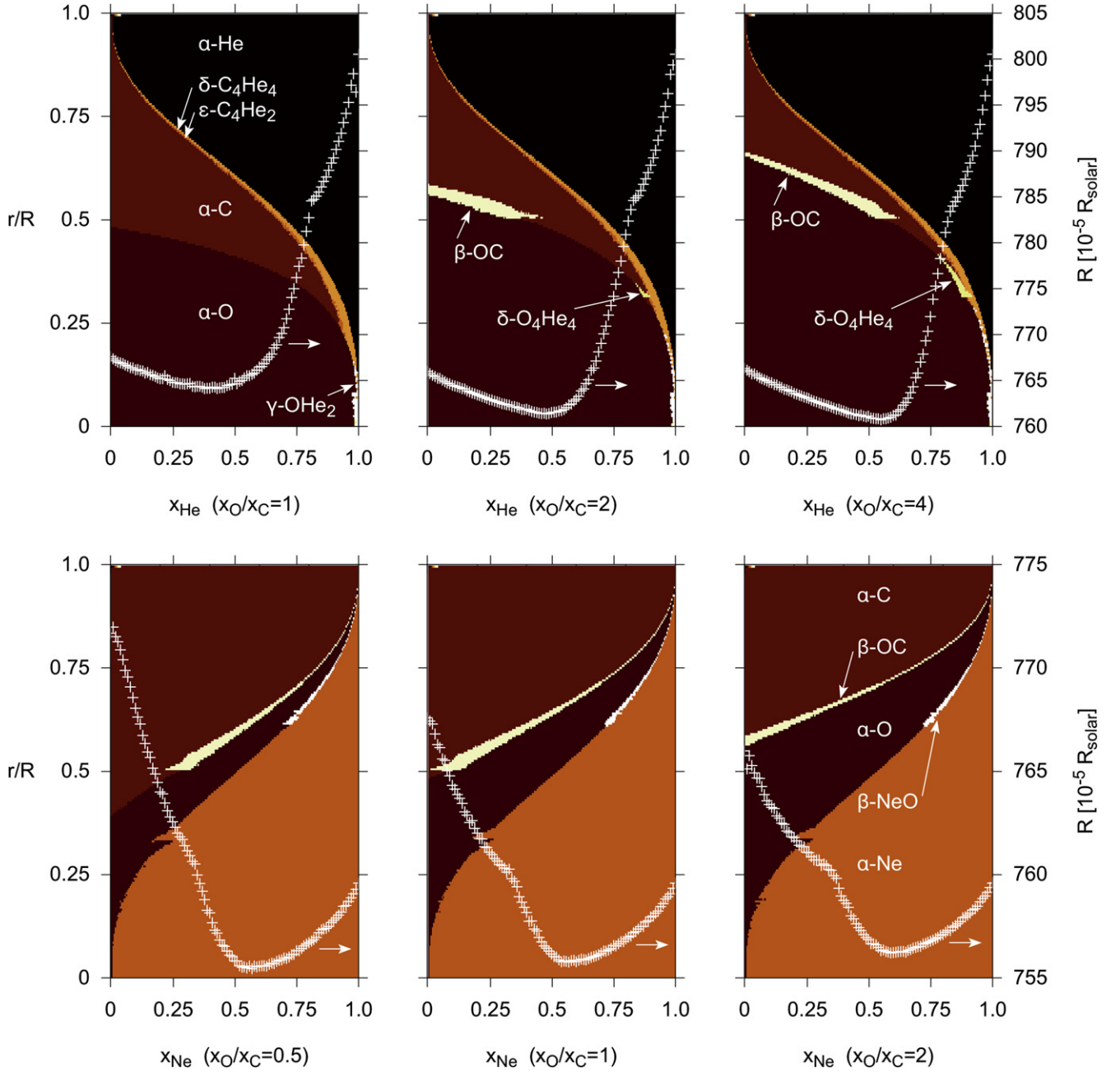
Figure 3. Equilibrium phase-layering diagrams for $1.0 M_\odot$, He–C–O WDs (top row) and $1.0 M_\odot$, C–O–Ne WDs (bottom row). Carbon–oxygen ratio is held at a fixed value in each panel, and mole fraction He or Ne makes up the balance. The discrete color map indicates the stable phases after one iteration of the procedure described in the main text. Further iterations produce no perceptible change in the layering diagram, save for an increase in the level of numerical noise. In cases where a given layer contains a two-phase mixture of bcc and a more complicated structure (these are the only types of mixture to occur), the color map indicates the more complicated phase. White plus signs give the stellar radius (right y-axis) as a function of composition, also after one iteration of the method. In the calculation of each layering diagram, 200 layers were used.

species is X, an additional set of linear constraints

$$0 = \sum_\alpha s_{X\alpha} n_{\alpha i} \quad \text{if } i < i_{\min}, \tag{15}$$

enforces the minimum radius $i_{\min}$ at which X can appear. This minimum allowed radius can then be incrementally stepped down, while the otherwise-unmodified equilibrium calculation is carried out at each step. We carry out a test of the method by settling $0.09 M_\odot$ of O on a $0.91 M_\odot$ He–C WD, and $0.1 M_\odot$ of Ne on a $0.9 M_\odot$ C–O WD. Overall compositions are fixed at

$x_{He} = 0.95$ with $x_C = x_O = 0.025$ and at $x_{Ne} = 0.07$ with $x_C = 2x_O = 0.62$, respectively; the final settled-out states are given by Figure 3. (Admittedly, these are not particularly realistic settling scenarios, but they serve as interesting test cases, forcing the presence of an interface between the highest and lowest Zs that otherwise does not happen in equilibrium.) In both settling scenarios, the out-of-equilibrium star contains one or more phases that do not appear in the final, equilibrium stacking sequence. One function of these extra phases is to serve as transient host structures for the settling

species: δ-O$_4$He$_4$ and γ-OHe$_2$ are hosts for settling oxygen, and θ-Ne$_2$C$_4$ is a host for settling neon. The phase-settling diagram for the He–O–C star is fairly nontrivial, with as many as seven distinct strata near $i_{min}/N_L \approx 0.25$. A minimum in the stellar radius appears around this point (as it also does in the O–C–Ne settling calculation), indicating that the lowest-enthalpy star is not the most compact star. This result hints at the prospects for new phenomena that are enabled by compositional and structural heterogeneity that takes advantage of the additional "chemical" degrees of freedom afforded by multinary phases.

8. FINITE TEMPERATURE

Here we give a brief, qualitative discussion of some effects that will become important at finite temperatures; a detailed analysis is a subject for future work. At finite T, the chemical potentials $\mu_\alpha(T, P_i)$ must be modified to account for phonons, smearing of the Fermi surface, associated smearing of the electron capture layers that will give an adjustment in composition, and if α denotes an alloy or solution phase, mixing entropy. Since the entropic part of these contributions does not enter into the enthalpy, it is not possible to self-consistently include thermal effects in our equilibrium phase-layering method, which relies on the enthalpy transformation. However, thermal effects could be included post hoc. For example, one could compute the phonon free energy of an interphase crystal such as δ-C$_4$He$_4$ along with that of the equivalent phase-separated α-C and α-He crystals, add this quantity to the $T = 0$ free energy, and predict whether the interphase tends to thicken or thin at finite T. A rough estimate based on phases' bulk moduli ($K = -VdP/dV$) suggests that the thermal (phonon) correction to the free energy will tend to increase the stability of the soft outer phase strata relative to the stiff innner strata, likely shifting the interphases slightly toward the stellar center. There is also a possibility for additional, particularly soft interphases to appear in the stacking sequence, if entropic terms are large enough to affect the phase competition that winnows the phases of Table 1 down to the phase layering in Figure 3. A phonon calculation would also yield the elastic tensor and help characterize the degree of elastic anisotropy as a function of depth, give a prediction for the relative melting temperatures via the Lindemann parameter (ratio of rms nucleus displacement to equilibrium lattice spacing), and provide the effective oscillator frequencies entering into pycnonuclear reaction rates. Finally, we note that the simple mechanical stability criterion used here should be replaced with the Ledoux criterion at finite T. See Reisenegger (2001) for an application to multicomponent neutron stars. Again, it is difficult to see how this more sophisticated criterion can be built into the current method, but it could at least be

checked after including thermal effects in the manner described.

REFERENCES

Abraham, N. L., & Probert, M. I. J. 2008, PhRvB, 77, 134117
American Society for Metals 1977, Atlas of Isothermal Transformation and Cooling Transformation Diagrams (Metals Park, OH: American Society for Metals)
Andersson, J. O., Helander, T., Höglund, L., Shi, P. F., & Sundman, B. 2002, Calphad, 26, 273
Baiko, D. A. 2002, PhRvE, 66, 056405
Barber, S. D., Patterson, A. J., Kilic, M., et al. 2012, ApJ, 760, 26
Chamel, N., & Haensel, P. 2008, LRR, 11, 10
Dyson, F. J. 1971, AnPhy, 63, 1
Engstrom, T. A., Crespi, V. H., Owen, B. J., et al. 2015, arXiv:1409.3299v2
Espósito, R. O., Castier, M., & Tavares, F. W. 2000, ChEnS, 55, 3495
Gale, J. D., & Rohl, A. L. 2003, MoSim, 29, 291
Gupta, S., Brown, E. F., Schatz, H., Möller, P., & Kratz, K.-L. 2007, ApJ, 662, 1188
Hillert, M. 2007, Phase Equilibria, Phase Diagrams and Phase Transformations (2nd ed.; Cambridge: Cambridge Univ. Press)
Hopkins, A. B., Jiao, Y., Stillinger, F. H., & Torquato, S. 2011, PhRvL, 107, 125501
Hopkins, A. B., Stillinger, F. H., & Torquato, S. 2012, PhRvE, 85, 021130
Horowitz, C. J., & Berry, D. K. 2009, PhRvC, 79, 065803
Horowitz, C. J., Berry, D. K., & Brown, E. F. 2007, PhRvE, 75, 066101
Horowitz, C. J., Caballero, O. L., & Berry, D. K. 2009, PhRvE, 79, 026103
Israel, G. L., Belloni, T., Stella, L., et al. 2005, ApJ, 628, 53
Johnson-McDaniel, N. K., & Owen, B. J. 2013, PhRvD, 88, 044004
Jordan, G. C., IV, Perets, H. B., Fisher, R. T., & Van Rossum, D. R. 2012, ApJL, 761, L23
Kobyakov, D., & Pethick, C. J. 2014, PhRvL, 112, 112504
Kozhberov, A. A., & Baiko, D. A. 2012, CoPP, 52, 153
Krill, C. E., III, & Chen, L.-Q. 2002, AcMat, 50, 3057
Lindblom, L. 1992, ApJ, 398, 569
Lindblom, L., Owen, B. J., & Ushomirsky, G. 2000, PhRvD, 62, 084030
Lonie, D. C., & Zurek, E. 2011, CoPhC, 182, 372
Medin, Z., & Cumming, A. 2010, PhRvE, 81, 036107
Oganov, A. R., & Glass, C. W. 2006, JChPh, 124, 244704
Ogata, S., & Ichimaru, S. 1990, PhRvA, 42, 4867
Perna, R., & Pons, J. A. 2011, ApJL, 727, L51
Pickard, C. J., & Needs, R. J. 2011, JPCM, 23, 053201
Pollock, E. L., & Hansen, J. P. 1973, PhRvA, 8, 3110
Rafikov, R. R. 2011, ApJL, 732, L3
Reisenegger, A. 2001, ApJ, 550, 860
Shen, K. J., & Bildsten, L. 2014, ApJ, 785, 61
Wang, Y., Lv, J., Zhu, L., & Ma, Y. 2010, PhRvB, 82, 094116
Wu, S. Q., Ji, M., Wang, C. Z., et al. 2014, JPCM, 26, 035402
Yakovlev, D. G., Gasques, L. R., Afanasjev, A. V., Beard, M., & Wiescher, M. 2006, PhRvC, 74, 035803